



# Weyl semimetals from noncentrosymmetric topological insulators

Jianpeng Liu and David Vanderbilt

*Department of Physics and Astronomy, Rutgers University, Piscataway, New Jersey 08854-8019, USA*

(Received 22 September 2014; published 28 October 2014)

We study the problem of phase transitions from three-dimensional topological to normal insulators without inversion symmetry. In contrast with the conclusions of some previous work, we show that a Weyl semimetal always exists as an intermediate phase regardless of any constraint from lattice symmetries, although the interval of the critical region is sensitive to the choice of path in the parameter space and can be very narrow. We demonstrate this behavior by carrying out first-principles calculations on the noncentrosymmetric topological insulators  $\text{LaBiTe}_3$  and  $\text{LuBiTe}_3$  and the trivial insulator  $\text{BiTeI}$ . We find that a robust Weyl-semimetal phase exists in the solid solutions  $\text{LaBi}_{1-x}\text{Sb}_x\text{Te}_3$  and  $\text{LuBi}_{1-x}\text{Sb}_x\text{Te}_3$  for  $x \approx 38.5\%–41.9\%$  and  $x \approx 40.5\%–45.1\%$ , respectively. A low-energy effective model is also constructed to describe the critical behavior in these two materials. In  $\text{BiTeI}$ , a Weyl semimetal also appears with applied pressure, but only within a very small pressure range, which may explain why it has not been experimentally observed.

DOI: [10.1103/PhysRevB.90.155316](https://doi.org/10.1103/PhysRevB.90.155316)

PACS number(s): 73.43.Nq, 73.20.At, 78.40.Kc

## I. INTRODUCTION

The significance of topology in determining electronic properties has become widely appreciated with the discovery of the integer quantum Hall effect and been highlighted further by the recent interest in topological insulators (TIs) [1–4]. In topological band theory, a topological index, such as the Chern number or the  $\mathbb{Z}_2$  index, is well defined only for gapped systems, and the topological character is signaled by the presence of novel gapless surface states which cannot exist in any isolated two-dimensional (2D) system [3,4]. Recently, the concept of topological phases is further generalized to three-dimensional (3D) bulk gapless systems, whose topological behavior is protected by lattice translational symmetry, known as the Weyl semimetal (WSM) [5–9].

A Weyl semimetal is characterized by a Fermi energy that intersects the bulk bands only at one or more pairs of band-touching points (BTPs) between nondegenerate valence and conduction bands. This can occur in the presence of spin-orbit coupling (SOC), typically in a crystal with broken time-reversal or inversion symmetry but not both, so that the pairs are of the form  $(\mathbf{k}_0, -\mathbf{k}_0)$  in the Brillouin zone (BZ). The effective Hamiltonian around a single BTP  $\mathbf{k}_0$  can be written as  $H(\mathbf{k}) = f_0(\mathbf{k}) + \mathbf{f}(\mathbf{k}) \cdot \boldsymbol{\sigma}$ , where  $f_0$  and  $\mathbf{f}$  are scalar and vector functions, respectively, of wave vector in the BZ and the  $\sigma_j$  are the Pauli matrices acting in the two-band space. If one expands the coefficient  $\mathbf{f}(\mathbf{k})$  to linear order around  $\mathbf{k}_0$ , one gets a Hamiltonian having the form of the Weyl Hamiltonian in relativistic quantum mechanics after a coordinate transformation in  $\mathbf{k}$  space. If the sign of the determinant of the Jacobian that describes the coordinate transformation is positive (negative), we call the BTP a Weyl node with positive (negative) chirality, and the low-energy excitations around such a Weyl node provide a condensed-matter realization of left-handed (right-handed) Weyl fermions.

These pairs of Weyl nodes are topologically protected in the sense that they are robust against small perturbations, which can be seen from the codimension argument as follows. One can introduce a parameter  $\lambda$  that acts as a perturbation on the BTP, and let both  $f_0$  and  $\mathbf{f}$  be dependent on  $\lambda$ . In order to get a band touching at  $(\mathbf{k}_0, \lambda_0)$ , the three coefficients

$\mathbf{f} \equiv (f_x, f_y, f_z)$  have to vanish. However, since there are four degrees of freedom, if  $\lambda_0 \rightarrow \lambda_0 + \delta\lambda$ , instead of opening a gap, the Weyl node would just shift slightly in momentum to compensate for the perturbation. In fact, there is no way to remove a Weyl node unless two Weyl nodes with opposite chirality annihilate each other.

If the two Weyl nodes are aligned in energy due to either time-reversal or some lattice symmetry, and the bands are filled right up to the Weyl nodes, then the Fermi energy would be locked there regardless of weak perturbations. That is, the Fermi level could be slightly shifted upward (downward) due to some weak perturbation, such that there is an electronlike (holelike) Fermi surface, then there must also be a holelike (electronlike) Fermi surface to conserve the total number of electrons, which is impossible in such a semimetal. It follows that the low-energy physics in the Weyl semimetal is completely dominated by the linearly dispersing states around the Weyl nodes, which leads to interesting surface states and transport properties.

The presence of Weyl nodes in the bulk band structure is responsible for the presence of Fermi arcs at the surface, which can be understood as follows [7,8]. Consider a small loop in the 2D surface BZ that encloses the projection along  $k_z$  of one Weyl point. When translated along  $k_z$ , this loop traces out a surface in the 3D BZ, and the application of Gauss's theorem implies that the Chern number on this surface must equal the chirality of the enclosed Weyl node. It follows that as  $(k_x, k_y)$  is carried around the loop, a single electron is pumped up to (or down from) the top surface, and this is only consistent with charge conservation if a single surface state crosses the Fermi energy  $E_F$  during the cycle. Since this argument applies for an arbitrary loop, surface states must exist at  $E_F$  along some arc emerging from the surface-projected Weyl point. If there is another Weyl node with opposite chirality, then the Chern number can vanish once the cylinder encloses both of the nodes, such that the Fermi arc would only extend between the two projected Weyl nodes [7,8]. It is also interesting to note that the surface states residing on the top and bottom surfaces disperse linearly in opposite directions and remain robust even when the Fermi energy deviates from the bulk Weyl nodes [10].

In a WSM with broken time-reversal (TR) symmetry, there is also a nonzero anomalous Hall conductivity (AHC) that is closely related to the positions of the Weyl nodes [11–13]. Consider the AHC  $\sigma_{xy}$  with the crystal oriented such that the third primitive reciprocal vector is along  $z$ . If we track the Chern number  $C_z$  of a 2D slice normal to  $z$  in the 3D BZ, we must find that it changes by  $\pm 1$  whenever  $k_z$  passes a Weyl node, with the sign depending on the chirality of the node. In the simplest case, if  $C_z = 1$  for  $k_z$  between the two Weyl nodes and zero elsewhere, then the AHC is just proportional to the separation of the two Weyl nodes in  $k_z$ . This is also interpreted as a consequence of the “chiral anomaly” in a WSM [14]. Other interesting transport phenomena can arise due to the chiral anomaly. For example, if a magnetic field  $\mathbf{B}$  is applied to a WSM in the  $z$  direction, Landau levels will be formed in the  $(x, y)$  plane. The zeroth Landau level disperses linearly along  $k_z$ , but in opposite directions for Weyl nodes with opposite chirality. As a result, if an electric field  $\mathbf{E}$  is applied along  $z$ , electrons would be pumped from one Weyl node to the other at a rate proportional to  $\mathbf{E} \cdot \mathbf{B}$ , with the Fermi arcs serving as a conduit [5,8,13,15].

As discussed above, a WSM requires the breaking of either TR or inversion symmetry. Many of the previous works are focused on WSMs without TR symmetry, such as in pyrochlore iridates [7], magnetically doped TI multilayers [12], and  $\text{Hg}_{1-x-y}\text{Cd}_x\text{Mn}_y\text{Te}$  [16]. In this paper, we study the WSM with preserved TR symmetry but broken inversion symmetry.

It was argued some time ago that the  $\mathbb{Z}_2$ -odd and  $\mathbb{Z}_2$ -even phases of a noncentrosymmetric insulator should always be bridged by a critical WSM phase [17,18]. If the transition is described by some adiabatic parameter  $\lambda$ , then as  $\lambda$  increases one expects first the appearance of  $m$  higher-order BTPs in the half BZ (and another  $m$  at the time-reversed points), where  $m = 1$  is typical of low-symmetry systems, while  $m > 1$  can occur when, e.g., rotational symmetries are present. These higher-order BTPs generally have quadratic dispersion in one direction while remaining linear in the other two, and are nonchiral; we refer to such a point henceforth as a “quadratic BTP.” As  $\lambda$  increases, each quadratic BTP splits to form a pair of Weyl nodes ( $4m$  altogether), which then migrate through the BZ and eventually annihilate at a second critical value of  $\lambda$  after exchanging partners. The previous work demonstrated that this process inverts the strong  $\mathbb{Z}_2$  index if  $m$  is odd [17,18]. Recently, however, Yang *et al.* claimed that for systems with certain high-symmetry lines in the BZ, the phase transition could occur at a unique critical value of  $\lambda$  at which the bands would touch and immediately reopen, instead of over some finite interval in  $\lambda$ , even when inversion symmetry is absent [19]. These authors suggested that BiTeI under pressure could serve as an example to support their claim [19,20].

In this paper, we address this issue carefully. We show that an intermediate critical WSM phase should always exist for any topological phase transition (TPT) between a normal and a  $\mathbb{Z}_2$ -odd insulating phase. We find, however, that the width of the critical WSM phase can be sensitive to the choice of path in parameter space and can sometimes be very small. To justify our conclusions, we take specific materials as examples. We first study the TPT in the solid solutions  $\text{LaBi}_{1-x}\text{Sb}_x\text{Te}_3$  and  $\text{LuBi}_{1-x}\text{Sb}_x\text{Te}_3$  using the virtual crystal approximation,

where the phase transition is driven by Sb substitution. The parent compounds at  $x = 100\%$ ,  $\text{LaBiTe}_3$  and  $\text{LuBiTe}_3$ , are hypothetical noncentrosymmetric materials that are predicted to be strong topological insulators in Ref. [21] and in the present work, respectively. Instead, the end members  $\text{LaSbTe}_3$  and  $\text{LuSbTe}_3$  at  $x = 0\%$  are trivial insulators [21]. We find that a WSM phase is obtained when  $x$  is in the range of about 38.5%–41.9% for  $\text{LaBiTe}_3$  and 40.5%–45.1% for  $\text{LuBiTe}_3$ . We further construct a low-energy effective model to describe the topological and phase-transitional behavior in this class of materials. We also revisit the TPT of BiTeI driven by applied pressure, where a WSM phase has not previously been observed [20,22]. Based on our calculations, we find that a small interval of WSM phase does actually intervene as increasing pressure drives the system from the trivial to the topological phase.

The paper is organized as follows. In Sec. II we derive the general behavior of TPTs in noncentrosymmetric insulators and point out some deficiencies in the discussion of BiTeI by Yang *et al.* [19]. In Sec. III we describe the lattice structures and basic topological properties of the materials, as well as the numerical methods used in the realistic-material calculations, especially the methods used in modeling the alloyed and pressurized systems and in searching for BTPs in the BZ. In Sec. IV we present the results for  $\text{LaBi}_{1-x}\text{Sb}_x\text{Te}_3$ ,  $\text{LuBi}_{1-x}\text{Sb}_x\text{Te}_3$ , and BiTeI, and discuss the sensitivity to the choice of path. In Sec. V, we summarize our work.

## II. TOPOLOGICAL TRANSITION IN NONCENTROSYMMETRIC INSULATORS

### A. General behavior

We consider the problem of TPTs in noncentrosymmetric insulators in the most general case. In the space of the two bands which touch at the TPT, the system can be described by the effective Hamiltonian

$$H(\mathbf{k}, \lambda) = f_x(\mathbf{k}, \lambda)\sigma_x + f_y(\mathbf{k}, \lambda)\sigma_y + f_z(\mathbf{k}, \lambda)\sigma_z, \quad (1)$$

where  $\lambda$  is the parameter that drives the TPT and  $\sigma_{x,y,z}$  are the three Pauli matrices defined in the space spanned by the highest occupied and the lowest unoccupied states at  $\mathbf{k}$ . Since we study the TPT between two insulating phases, we can assume without loss of generality that the system is gapped for  $\lambda < \lambda_0$ , and that the first touching that occurs at  $\lambda = \lambda_0$  takes place at  $\mathbf{k} = \mathbf{k}_0$ . In other words,  $f_i(\mathbf{k}_0, \lambda_0) = 0, i = x, y, z$ . Then we ask what happens if  $\mathbf{k}_0 \rightarrow \mathbf{k}_0 + \mathbf{q}$  and  $\lambda_0 \rightarrow \lambda_0 + \delta\lambda$ .

We first expand the coefficients  $\mathbf{f}$  around  $(\mathbf{k}_0, \lambda_0)$  as  $\mathbf{f} = \mathbf{J} \cdot \mathbf{q} + \mathbf{\Lambda} \delta\lambda$ , where  $\mathbf{q} = \mathbf{k} - \mathbf{k}_0, \delta\lambda = \lambda - \lambda_0, \mathbf{J}$  is the Jacobian with matrix elements  $J_{ij} = (\partial f_i / \partial k_j)|_{\mathbf{k}_0, \lambda_0}$ , and  $\mathbf{\Lambda}$  is a three vector with components  $\Lambda_i = (\partial f_i / \partial \lambda)|_{\mathbf{k}_0, \lambda_0}$ . A natural set of momentum-space coordinates can be defined in terms of the eigensystem  $\mathbf{J} \cdot \mathbf{v}_i = J_i \mathbf{v}_i$ . Defining  $\mathbf{q} = \sum_i p_i \mathbf{v}_i$  and  $\mathbf{u}_i = J_i \mathbf{v}_i$ , we obtain

$$\mathbf{f} = \sum_{i=1}^3 p_i \mathbf{u}_i + \delta\lambda \mathbf{\Lambda}. \quad (2)$$

Following the argument of Yang *et al.* [19], the Jacobian matrix  $\mathbf{J}$  has to be singular at  $(\mathbf{k}_0, \lambda_0)$  because otherwise there would be band touching even when  $\lambda < \lambda_0$ , contradicting

the assumption that the system is insulating for  $\lambda < \lambda_0$ . This implies that at least one of the eigenvalues of  $\mathbf{J}$  is zero. We assume for the moment that the others are nonzero, i.e., that  $\mathbf{J}$  is rank two, and let it be the first eigenvalue that vanishes. Since the  $p_1$ -dependence of  $\mathbf{f}$  then vanishes at linear order, we again follow Ref. [19] by including a second-order term to obtain

$$\mathbf{f} = p_2 \mathbf{u}_2 + p_3 \mathbf{u}_3 + \delta\lambda \mathbf{\Lambda} + p_1^2 \mathbf{w}, \quad (3)$$

where  $\mathbf{w} = (1/2)\partial^2 \mathbf{f} / \partial p_i \partial p_j |_{\mathbf{k}_0, \lambda_0}$ . Now we also have the freedom to carry out an arbitrary rotation in the pseudospin representation of the two-band space. That is, we redefine  $f_i$  to be the component in the pseudospin direction  $\mathbf{e}_i$ , with  $\mathbf{e}_3$  given by  $(\mathbf{u}_2 \times \mathbf{u}_3) / |\mathbf{u}_2 \times \mathbf{u}_3|$ , and  $\mathbf{e}_1$  and  $\mathbf{e}_2$  chosen to form an orthonormal frame with  $\mathbf{e}_3$ . Then  $u_{23}$  and  $u_{33}$  vanish, and we can write explicitly that

$$\begin{aligned} f_1 &= p_2 u_{21} + p_3 u_{31} + \delta\lambda \Lambda_1 + p_1^2 w_1, \\ f_2 &= p_2 u_{22} + p_3 u_{32} + \delta\lambda \Lambda_2 + p_1^2 w_2, \\ f_3 &= \delta\lambda \Lambda_3 + p_1^2 w_3. \end{aligned} \quad (4)$$

We assume  $\Lambda_3/w_3 < 0$ , since otherwise there are solutions at negative  $\lambda$ . Then at positive  $\lambda$ , there are always two solutions  $p_1 = \pm \sqrt{-\delta\lambda \Lambda_3 / w_3}$  at which  $f_3 = 0$ . Plugging this into the expressions for  $f_1$  and  $f_2$  in Eq. (4), we can obtain  $p_2$  and  $p_3$  by solving the linear system

$$\begin{bmatrix} u_{21} & u_{31} \\ u_{22} & u_{32} \end{bmatrix} \begin{bmatrix} p_2 \\ p_3 \end{bmatrix} + \begin{bmatrix} \Lambda_1 - w_1 \Lambda_3 / w_3 \\ \Lambda_2 - w_2 \Lambda_3 / w_3 \end{bmatrix} \delta\lambda = 0. \quad (5)$$

Solutions of the above equation always exist as long as the Jacobian matrix  $\mathbf{J}$  is of rank two, which means a critical WSM should always exist in the absence of a special lattice symmetry that would lower the rank of  $\mathbf{J}$ . From the above it also follows that at the critical  $\lambda = \lambda_0$  the dispersion around  $\mathbf{k}_0$  is quadratic in  $p_1$  and linear in  $p_2$  and  $p_3$ , and that for larger  $\lambda$  the Weyl point displacements scale like  $|p_1| \sim \sqrt{\delta\lambda}$  and  $|p_{2,3}| \sim \delta\lambda$ . The same conclusions in the rank-two case have been obtained by Murakami *et al.* [17] and restated by Yang *et al.* [19].

If the Jacobian matrix  $\mathbf{J}$  turns out to be rank one instead at  $\lambda_0$ , then the bands would first close at a doubly quadratic BTP. That is, there would be two vanishing eigenvalues of the Jacobian matrix (which we take to be the first and second), and the dispersion would be quadratic in  $p_1$  and  $p_2$  and linear in  $p_3$ . This implies that only the second-order terms associated with  $p_1$  and  $p_2$  need to be included in Eq. (3), yielding

$$\begin{aligned} f_1 &= p_3 u_{31} + \delta\lambda \Lambda_1 + p_1^2 w_1^{11} + p_2^2 w_1^{22} + 2p_1 p_2 w_1^{12}, \\ f_2 &= p_3 u_{32} + \delta\lambda \Lambda_2 + p_1^2 w_2^{11} + p_2^2 w_2^{22} + 2p_1 p_2 w_2^{12}, \\ f_3 &= p_3 u_{33} + \delta\lambda \Lambda_3 + p_1^2 w_3^{11} + p_2^2 w_3^{22} + 2p_1 p_2 w_3^{12}, \end{aligned} \quad (6)$$

where  $\mathbf{w}^{ij} = (1/2)\partial^2 \mathbf{f} / \partial p_i \partial p_j |_{\mathbf{k}_0, \lambda_0}$  ( $i, j = 1, 2$ ). We can make a similar transformation on  $\mathbf{f}$  such that the  $f_3$  direction is  $\mathbf{e}_3 = (\mathbf{u}_3 \times \mathbf{w}^{22}) / |\mathbf{u}_3 \times \mathbf{w}^{22}|$ , so that  $f_3$  becomes independent of  $p_3$  and  $p_2^2$ . Then one also has the freedom to rotate the  $p_1$  and  $p_2$  components to make  $w_3^{12}$  vanish. After these two transformations,  $f_3$  only depends on  $p_1^2$  and  $\delta\lambda$ , and one expects solutions at  $p_1 = \pm \sqrt{-\delta\lambda \Lambda_3 / w_3^{11}}$ . Plugging this into the expressions for  $f_1$  and  $f_2$  in Eq. (6), one obtains a quadratic equation for  $p_2$  of the form  $a\delta\lambda + bp_2^2 + c\sqrt{\delta\lambda}p_2 = 0$ , where  $a$ ,  $b$ , and  $c$  are some constants determined by the components

of  $\mathbf{u}_3$ ,  $\mathbf{\Lambda}$ , and  $\mathbf{w}^{ij}$  ( $i, j = 1, 2$ ). If there are real solutions for the above equation, then the doubly quadratic BTPs would split into four Weyl nodes whose trajectories scale as  $p_1 \sim \pm \sqrt{\delta\lambda}$  and  $p_2 \sim \pm \sqrt{\delta\lambda}$ ,  $p_3 \sim \delta\lambda$ . Otherwise, if there is no solution for  $p_2$ , a gap would be opened up immediately after the band touching at  $(\mathbf{k}_0, \lambda_0)$ , which would represent the rare case of an “insulator-insulator transition” using the language of Ref. [19].

However, we do not expect that the strong  $\mathbb{Z}_2$  index would be inverted for such an insulator-insulator transition in the rank-one case. This can be seen as follows. If the BTP does not lie in any of the TR-invariant slices ( $k_j = \{0, \pi\}$ ,  $j = 1, 2, 3$ ), then certainly the 2D  $\mathbb{Z}_2$  indices of the TR invariant slices would not change, and it follows that none of the four 3D  $\mathbb{Z}_2$  indices would change either. If the BTP happens to reside in one of the TR invariant slices, then since the dispersion in the 2D slice must be quadratic in at least one direction, it should be topologically equivalent to the superposition of an even number of linearly dispersing Weyl nodes, which is also not expected to flip the 2D  $\mathbb{Z}_2$  index, as argued in Ref. [17]. Thus none of the 3D  $\mathbb{Z}_2$  indices, including the strong index, would change.

To summarize this section, we find without any lattice-symmetry restriction that a critical WSM phase always exists in the rank-two case. In the rank-one case, an insulator-insulator type transition is allowed in principle, but would not be expected to be accompanied by a change in the strong  $\mathbb{Z}_2$  index. Therefore, it is fair to claim that, regardless of special lattice symmetry, there is always a WSM phase connecting  $\mathbb{Z}_2$ -odd and  $\mathbb{Z}_2$ -even phases in a noncentrosymmetric insulator.

## B. Discussion of BiTeI

In this section we discuss the TPT in pressured BiTeI, a case in which the TPT is driven in a system with  $C_{3v}$  symmetry. Contrary to the conclusions of Ref. [19], here we argue that a critical WSM does exist in the TPT of BiTeI, although the pressure interval over which it occurs may be rather narrow.

In Refs. [19,20] the authors argued that if there exists a high-symmetry line in the BZ such that the dispersion extremum evolves along the line as a function of the adiabatic parameter (pressure), then one could get an insulator-insulator type transition without going through a critical WSM. The authors further pointed out that the high-symmetry lines from  $A$  to  $H$  in the BZ of BiTeI, shown in Fig. 1(d), satisfy some necessary conditions for this to occur. Moreover, they showed that the symmetry of BiTeI is such that if one concentrates on the band dispersions along these  $A-H$  lines, one finds a pair of extrema (one valence-band maximum and one conduction-band minimum) which migrate along the  $A-H$  line as a function of the external parameter (pressure), coincide at a critical value, and then separate again to reopen the gap. They furthermore showed that the dispersions are quadratic in the two orthogonal directions (except exactly at the critical value), raising the possibility that the extrema in question could be minima and maxima in all three  $k$ -space directions. This would correspond to the insulator-insulator transition without an intervening WSM phase. However, our analysis in the previous section shows that this cannot occur in the rank-two case, and that the extrema in question actually become saddle points after the band touchings occur along the  $A-H$  lines. In this case, as recognized in Ref. [19], a WSM phase does occur.

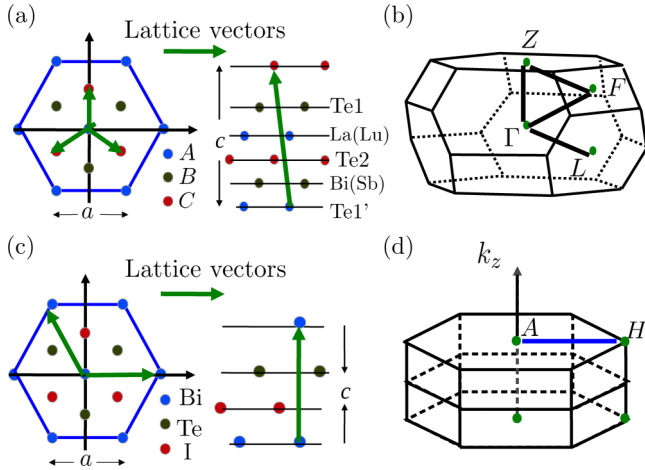


FIG. 1. (Color online) (a) The lattice structure of  $\text{LaBiTe}_3$ ,  $\text{LuBiTe}_3$ ,  $\text{LaSbTe}_3$ , and  $\text{LuSbTe}_3$ . (b) The BZ of  $\text{La(Lu)Bi(Sb)Te}_3$ . (c) The lattice structure of  $\text{BiTeI}$ . (d) The BZ of  $\text{BiTeI}$ .

As has been verified in Ref. [19], the Jacobian does remain of rank two on these lines in  $\text{BiTeI}$ , and we shall show below in Sec. IV B that an intermediate WSM phase does occur. We also point out that Fig. 2 of Ref. [19] does not demonstrate the absence of the Weyl nodes, since they are expected to lie off the  $(k_x, k_z)$  plane on which the dispersion was plotted.

Yang *et al.* [19] gave another argument in favor of the insulator-insulator scenario in  $\text{BiTeI}$  as follows. They noted that the band touching first takes place on the  $A$ - $H$  line, which is invariant under the combination of time-reversal and mirror operations. This imposes some constraints on the form of the effective Hamiltonian around the BTP, and from these the authors concluded that, if Weyl nodes do appear, they should migrate along trajectories of the form  $p_1 \sim \pm\delta\lambda^{1/2}$ ,  $p_2 \sim \pm\delta\lambda^{3/2}$ , and  $p_3 \sim \delta\lambda$ . Such a curve in 3D space possesses nonzero torsion, so that the trajectories of the two Weyl nodes emerging from one quadratic BTP could never join again and form a closed curve. This implies that if the WSM is formed by such an event, then it would remain permanently, contradicting the fact that  $\text{BiTeI}$  clearly becomes a globally gapped TI at higher pressures. Based on this reasoning, they concluded that the TPT in  $\text{BiTeI}$  must be an insulator-insulator transition without an intermediate WSM.

However, this argument neglects the fact that the  $C_{3v}$  symmetry means that there are several  $A$ - $H$  lines in the BZ of  $\text{BiTeI}$ , and the gap first closes by the simultaneous appearance of quadratic BTPs at equivalent positions on all of these lines. Even though the two Weyl nodes which emerge from a single quadratic BTP cannot meet each other, as shown from the torsion of their trajectories, the Weyl nodes from different BTPs can interchange partners and eventually annihilate each other in such a way as to form a closed curve in the BZ. This is exactly the mechanism of the topological phase transition in noncentrosymmetric TIs [17,18]. As will be discussed in Sec. IV B, there are actually six quadratic BTPs in the full BZ that appear simultaneously, according to the crystalline and TR symmetries. These six Dirac nodes split into 12 Weyl nodes, which are eventually gapped out by annihilation after exchanging partners.

In the following section, we will study the TPTs in various inversion asymmetric materials by first-principles calculations. We predict  $\text{LaBi}_{1-x}\text{Sb}_x\text{Te}_3$  and  $\text{LuBi}_{1-x}\text{Sb}_x\text{Te}_3$  to be WSM candidates within a certain range of impurity composition  $x$ . We also revisit the case of  $\text{BiTeI}$ , and find that a WSM phase emerges when external pressure is applied to  $\text{BiTeI}$ , but only within a small pressure interval.

### III. PRELIMINARIES

#### A. Lattice structures and basic topological properties

The assumed crystal structures of  $\text{LaBiTe}_3$  and  $\text{LuBiTe}_3$  are very similar to  $\text{Bi}_2\text{Te}_3$ , where five atomic monolayers stack in the  $[111]$  direction in an  $A$ - $B$ - $C$ - $A$ -... sequence forming quintuple layers (QLs) as shown in Fig. 1(a). The only difference is that one of the two Bi atoms in the primitive unit cell is replaced by a La or Lu atom, which breaks the inversion symmetry. The lattice structure of  $\text{LaSbTe}_3$  and  $\text{LuSbTe}_3$  is the same as for  $\text{LaBiTe}_3$  and  $\text{LuBiTe}_3$ , except that all the Bi atoms are substituted by Sb. The in-plane hexagonal lattice parameters for  $\text{LaBiTe}_3$  and  $\text{LuBiTe}_3$  are  $a = 4.39 \text{ \AA}$  and  $4.18 \text{ \AA}$ , respectively, while the size of a QL along  $c$  is  $10.07$  and  $10.29 \text{ \AA}$ , respectively. The lattice parameters of  $\text{LaSbTe}_3$  are slightly different from  $\text{LaBiTe}_3$ , with  $a = 4.24 \text{ \AA}$  and  $c = 10.13 \text{ \AA}$ . The lattice parameters for  $\text{LuSbTe}_3$  have not been reported before, so we use those from  $\text{LuBiTe}_3$ . Among these four hypothetical materials,  $\text{LaBiTe}_3$  has been previously reported as a candidate for an inversion-asymmetric TI [21].  $\text{LuBiTe}_3$  is first reported as a TI candidate in this paper; the nontrivial band topology is confirmed by calculating the bulk  $\mathbb{Z}_2$  index [23] and checking the existence of topological surface states. On the other hand,  $\text{LaSbTe}_3$  and  $\text{LuSbTe}_3$  are trivial insulators.

As shown in Fig. 1(c),  $\text{BiTeI}$  has a hexagonal lattice structure with three atoms in the primitive cell stacked as  $A$ - $B$ - $C$ - $A$ -... along the  $z$  direction. The lattice parameters in plane and along the hexagonal axis are  $a = 4.339 \text{ \AA}$  and  $c = 6.854 \text{ \AA}$ .  $\text{BiTeI}$  itself is a trivial insulator with a large Rashba spin splitting in the bulk [24], but it can be driven into a TI state by applying pressure. Previous studies have suggested that the transition to the topological phase is not mediated by a WSM phase [19,20], but we revisit this issue in Sec. IV B and come to different conclusions.

#### B. First-principles methodology

We carry out the bulk first-principles calculations using the VASP package including SOC [25,26]. The generalized-gradient approximation is used to treat the exchange-correlation functional [27,28]. The BZ is sampled on an  $8 \times 8 \times 8$  Monkhorst-Pack [29]  $\mathbf{k}$  mesh and an energy cutoff of  $340 \text{ eV}$  is used. The output from the first-principles plane-wave calculations are then interfaced to the WANNIER90 package [30] to construct realistic tight-binding (TB) models for these materials [31].

To describe the electronic structure of  $\text{LaBi}_{1-x}\text{Sb}_x\text{Te}_3$  and  $\text{LuBi}_{1-x}\text{Sb}_x\text{Te}_3$ , we adopt the virtual crystal approximation (VCA) in which each Bi or Sb is replaced by a ‘‘virtual’’ atom whose properties are a weighted average of the two constituents. The VCA treatment typically gives a reasonable description for solid-solution systems in which the dopant and

host atoms have a similar chemical character. For example, the VCA was shown to work well in describing Sb substitution in  $\text{Bi}_2\text{Se}_3$ , because of the similar orbital character of Sb  $5p$  and Bi  $6p$ , but not for In substitution, where In  $5s$  orbitals become involved [32]. The VCA is implemented in the Wannier basis by constructing separate 36-band models for  $\text{LaBiTe}_3$  ( $\text{LuBiTe}_3$ ) and  $\text{LaSbTe}_3$  ( $\text{LuSbTe}_3$ ), including all the valence  $p$  orbitals of the cations and anions, as well as the  $5d$  and  $6s$  orbitals of the rare-earth elements [33]. In the solid solution, the Hamiltonian matrix elements are then taken as a linear interpolation in impurity composition  $x$  of the corresponding matrix elements of the parent materials. That is, we take  $H_{mn}^{\text{VCA}} = (1-x)H_{mn}^{\text{Bi}} + xH_{mn}^{\text{Sb}}$ , where  $H_{mn}^{\text{Bi}}$  and  $H_{mn}^{\text{Sb}}$  denote the matrix elements of the TB models of  $\text{LaBiTe}_3$  and  $\text{LaSbTe}_3$ . It worth noting that when generating the Wannier functions (WFs) for the VCA treatment, the Wannier basis functions have to be chosen as similar as possible before the averaging [32]. We therefore use WF's that are constructed simply by projecting the Bloch states onto the same set of atomiclike trial orbitals without applying a subsequent maximal-localization procedure [34,35].

Similarly, to study the pressure-induced TPT in  $\text{BiTeI}$ , we carry out first-principles calculations for the system at the zero-pressure volume, where it is topologically normal, and also at 85.4% of the original volume, a value chosen somewhat arbitrarily to be well inside the TI region [20]. We denote these two states as  $\eta = 0$  and  $\eta = 1$ , respectively. Then from the Wannier representation we again construct a realistic Hamiltonian for each system, denoted as  $H_0$  and  $H_1$ , respectively, including all the valence  $p$  orbitals of Bi, Te, and I. Finally we linearly interpolate these as  $H(\eta) = (1-\eta)H_0 + \eta H_1$ , treating  $\eta$  as an adiabatic parameter that tunes the system through the topological phase transition.

Using these Wannierized effective TB models, we can search for BTPs very efficiently over the entire BZ. We first sample the irreducible BZ using a relatively sparse  $\mathbf{k}$  mesh, e.g.,  $20 \times 20 \times 20$ , and find the point  $\mathbf{k}_0$  having the smallest direct band gap on this mesh. A second-round search is conducted by scanning over a denser  $\mathbf{k}$  mesh within a sphere centered on  $\mathbf{k}_0$ . We then repeat the procedure iteratively until convergence is reached. All of the trajectories of Weyl nodes presented in Sec. IV are obtained using this approach.

## IV. RESULTS

### A. $\text{LaBi}_{1-x}\text{Sb}_x\text{Te}_3$ and $\text{LuBi}_{1-x}\text{Sb}_x\text{Te}_3$

#### 1. Band gap and Weyl chirality

For each of these materials we scan over a mesh in composition  $x$ , and for each  $x$  we construct the Wannierized Hamiltonian for the corresponding solid solution within the VCA. We then use the methods of the previous section to search for the BTPs in the entire irreducible BZ. Plots of the smallest direct band gap in the BZ vs  $x$  are presented in Fig. 2. Clearly the gap remains closed over a finite range of  $x$  in both cases, from 38.5% to 41.9% for  $\text{LaBi}_{1-x}\text{Sb}_x\text{Te}_3$  and 40.5% to 45.1% for  $\text{LuBi}_{1-x}\text{Sb}_x\text{Te}_3$ . By checking the dispersion around the gap-closure point, we confirm that the system is semimetallic with the Fermi level lying at a set of degenerate Weyl BTPs over this entire range.

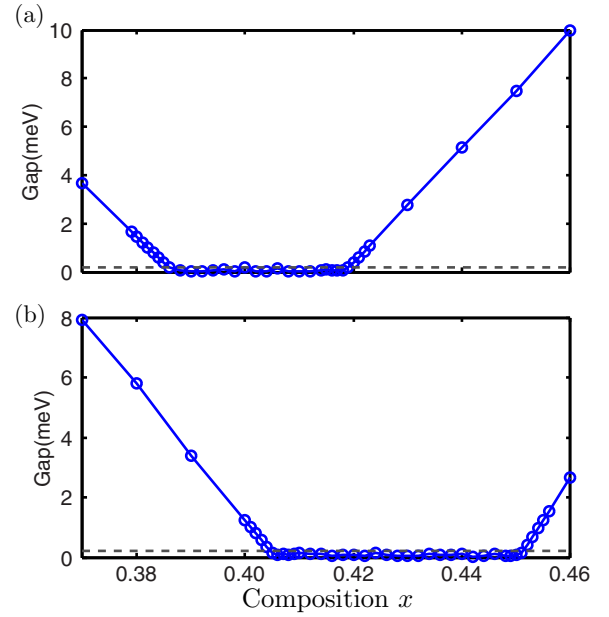


FIG. 2. (Color online) Smallest direct band gap in the BZ vs composition  $x$  for (a)  $\text{LaBi}_{1-x}\text{Sb}_x\text{Te}_3$  and (b)  $\text{LuBi}_{1-x}\text{Sb}_x\text{Te}_3$ . Dashed gray line marks our chosen threshold of 0.2 meV to signal a gap closure.

To illustrate the topological character, we further calculate the chirality of the BTPs, which is given by the determinant of the Jacobian matrix  $J_{ij} = \partial f_i / \partial k_j$ . Figure 3 shows how  $\det(\mathbf{J})$  varies with  $x$  for the BTPs in  $\text{LaBi}_{1-x}\text{Sb}_x\text{Te}_3$  and  $\text{LuBi}_{1-x}\text{Sb}_x\text{Te}_3$ . The red and black open circles mark the values of  $\det(\mathbf{J})$  for the BTPs with positive and negative chirality, which are mapped into each other by mirror operations about the  $k_x = 0$  and other equivalent mirror planes. One can see that at the beginning of the band touching, the chirality starts at zero, indicating the creation of a quadratic

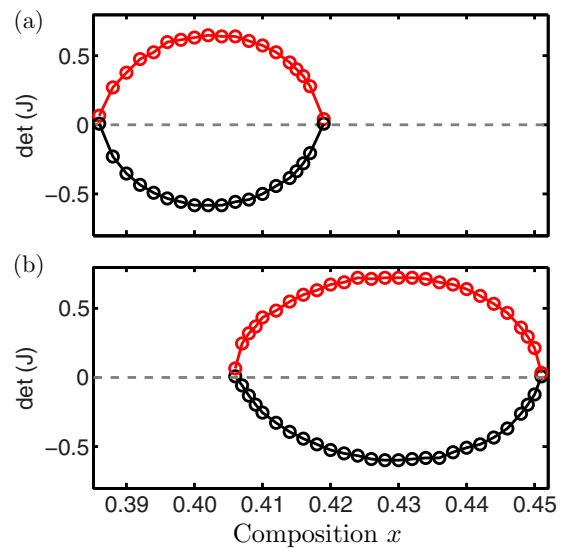


FIG. 3. (Color online) Determinant of the Jacobian matrix evaluated at Weyl nodes with positive (red) and negative (black) chirality vs composition  $x$ , for (a)  $\text{LaBi}_{1-x}\text{Sb}_x\text{Te}_3$  and (b)  $\text{LuBi}_{1-x}\text{Sb}_x\text{Te}_3$ .

BTP. As  $x$  increases, each quadratic BTP splits into two Weyl nodes with opposite chirality. These then migrate through the BZ and eventually annihilate each other at the point where the chirality returns to zero.

### 2. Symmetry considerations

As mentioned earlier, the point group of this class of materials is  $C_{3v}$ , which has a threefold rotation axis along  $k_z$  and three mirror planes that contain the  $k_z$  axis and intersect the  $k_z=0$  plane on the lines  $k_x=0$  and  $k_y=\pm k_x/\sqrt{3}$ . We define an azimuthal angle  $\theta$  that measures the rotation of  $(k_x, k_y)$  from the  $+k_y$  axis in the clockwise direction as shown in Fig. 4(a). As a result of the threefold rotational symmetry, if a Weyl node with positive chirality appears at some  $\theta$  in the region  $0 \leq \theta \leq \pi/3$  and at some  $k_z$  in the upper half BZ, then there must be another two nodes with the same chirality and the same  $k_z$  located at  $\theta + 2\pi/3$  and  $\theta - 2\pi/3$ . Taking into account the mirror symmetry, these must have negative-chirality partners at the same  $k_z$  but at  $-\theta$ ,  $-\theta + 2\pi/3$ , and  $-\theta - 2\pi/3$ .

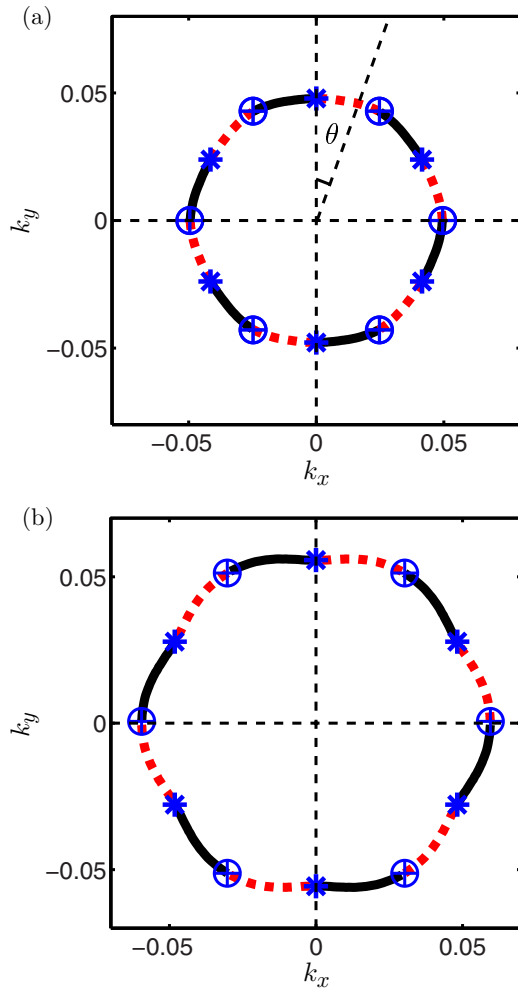


FIG. 4. (Color online) Trajectories of Weyl nodes in the  $(k_x, k_y)$  plane (in units of  $\text{\AA}^{-1}$ ). Dashed red lines indicate Weyl nodes of positive chirality; solid black lines are negative. The “\*” and “⊕” denote, respectively, the points of creation or annihilation of Weyl nodes. (a) For  $\text{LaBi}_{1-x}\text{Sb}_x\text{Te}_3$ . (b) For  $\text{LuBi}_{1-x}\text{Sb}_x\text{Te}_3$ .

Finally, because of TR symmetry, each Weyl node at  $\mathbf{k}$  is always accompanied by another at  $-\mathbf{k}$  with the same chirality, giving six more Weyl nodes in the lower half BZ. We thus generically expect a total of 12 Weyl nodes in the entire BZ for compositions  $x$  in the region of the WSM phase.

### 3. Weyl trajectories

Figure 4 shows the trajectories of the Weyl nodes in  $\text{LaBi}_{1-x}\text{Sb}_x\text{Te}_3$  and  $\text{LuBi}_{1-x}\text{Sb}_x\text{Te}_3$  projected onto the  $(k_x, k_y)$  plane as  $x$  passes through the critical region. The red dashed line represents the trajectory of Weyl nodes with positive chirality, while the solid black one denotes those with negative chirality, and the “\*” and “⊕” denote the creation and annihilation points of the Weyl nodes, respectively. As  $x$  increases, six quadratic BTPs are simultaneously created in the mirror planes; this occurs at  $x_{c1} = 38.5\%$  for  $\text{LaBi}_{1-x}\text{Sb}_x\text{Te}_3$  and  $40.5\%$  for  $\text{LuBi}_{1-x}\text{Sb}_x\text{Te}_3$ . Each quadratic BTP then splits into two Weyl nodes of opposite chirality, and these 12 nodes migrate along the solid black and dashed red lines shown in the figure. Eventually, after exchanging partners, the Weyl nodes meet and annihilate each other in another set of high-symmetry planes ( $k_y=0$  and other equivalent planes), at  $x_{c2} = 41.9\%$  for  $\text{LaBi}_{1-x}\text{Sb}_x\text{Te}_3$  and  $45.1\%$  for  $\text{LuBi}_{1-x}\text{Sb}_x\text{Te}_3$ .

Figures 5(a) and 5(b) show the trajectory of the Weyl nodes in the  $k_z$  direction. At  $x = x_{c1}$ , six quadratic BTPs are created, three in the top half-BZ and three in the bottom half-BZ, but all of them fairly close to the BZ boundary plane at  $k_z = \pm\pi/c$ . As  $x$  increases, the six BTPs split to form 12 Weyl nodes, and these begin to move toward the above-mentioned BZ boundary plane. Finally, after interchanging partners, Weyl nodes of opposite chirality annihilate in pairs at  $x_{c2}$  on the BZ boundary

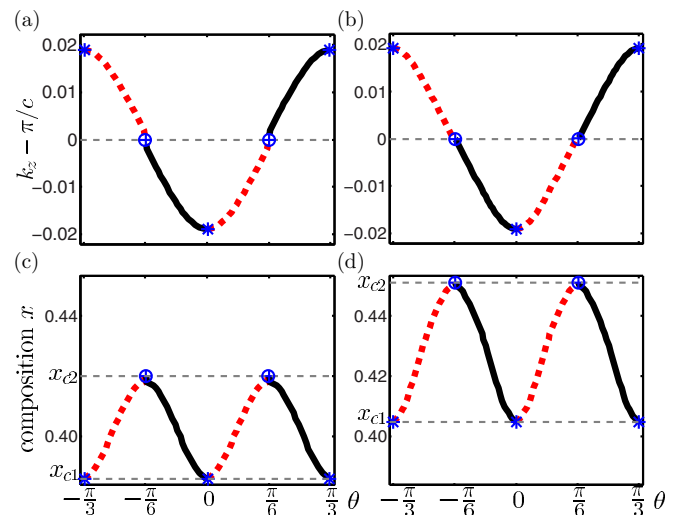


FIG. 5. (Color online) (a), (b) Trajectories of Weyl nodes in the  $k_z$  direction (in units of  $\text{\AA}^{-1}$ ) for (a)  $\text{LaBi}_{1-x}\text{Sb}_x\text{Te}_3$  and (b)  $\text{LuBi}_{1-x}\text{Sb}_x\text{Te}_3$ . Dashed red (solid black) lines refer to the Weyl nodes with positive (negative) chirality.  $\theta$  is the azimuthal angle in the  $(k_x, k_y)$  plane, as indicated in Fig. 4(a). The “\*” and “⊕” denote the creation and annihilation point of the Weyl nodes, respectively. (c), (d) Trajectories of Weyl nodes in the direction of impurity composition  $x$  for (c)  $\text{LaBi}_{1-x}\text{Sb}_x\text{Te}_3$  and (d)  $\text{LuBi}_{1-x}\text{Sb}_x\text{Te}_3$ .

plane at  $k_z = \pm\pi/c$ . For  $x > x_{c2}$  a global gap opens up and the system is again an insulator but with an inverted  $\mathbb{Z}_2$  index.

The locus of Weyl points can be regarded as forming a loop in the four-dimensional space of  $(k_x, k_y, k_z, x)$ , and just as this loop can be projected onto  $k_z$  as in Figs. 5(a) and 5(b), it can also be projected onto the direction of impurity composition  $x$  as shown in Figs. 5(c) and 5(d). Again, it is clear that the Weyl nodes are created at  $x_{c1}$  in the mirror planes and annihilated at  $x_{c2}$  at  $\theta = \pm\pi/6$ . These plots may also be helpful in seeing how the high sixfold symmetry contributes to the narrowness of the WSM region. If the symmetry of the system were lower, the period of oscillation in  $\theta$  in Figs. 5(c) and 5(d) would be longer, which would allow the Weyl nodes to oscillate farther in the  $x$  direction, giving a wider window of concentration for the WSM phase. In contrast, a fictitious system with an  $N$ -fold rotational symmetry would force the width of the WSM region to vanish as  $N \rightarrow \infty$ . Here we have  $N = 6$ , which is evidently large enough to limit the WSM phase to a rather small interval in  $x$ .

#### 4. Surface Fermi arcs

One of the most characteristic features of WSMs is the existence of Fermi arcs in the surface band structure. Here we calculate the surface states using the surface Green's-function technique [36], which is implemented in the context of the VCA effective Hamiltonian in the Wannier basis. The surface BZ is sampled by a  $64 \times 64$   $\mathbf{k}$  mesh, and the surface spectral functions calculated on this mesh are then linearly interpolated to fit a  $128 \times 128$   $\mathbf{k}$  mesh. Figure 6 shows the normalized

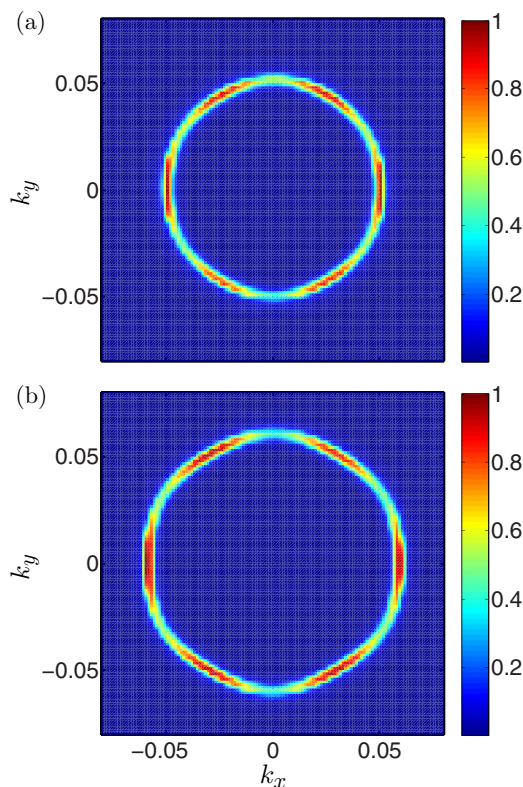


FIG. 6. (Color online) Surface spectral function averaged around the Fermi level ( $k_x$  and  $k_y$  in units of  $\text{\AA}^{-1}$ ) for (a)  $\text{LaBi}_{1-x}\text{Sb}_x\text{Te}_3$  at  $x = 0.405$  and (b)  $\text{LuBi}_{1-x}\text{Sb}_x\text{Te}_3$  at  $x = 0.43$ .

surface spectral functions averaged around the Fermi level for  $\text{LaBi}_{1-x}\text{Sb}_x\text{Te}_3$  at  $x = 0.405$  and for  $\text{LuBi}_{1-x}\text{Sb}_x\text{Te}_3$  at  $x = 0.43$ . The averaging is done over an energy window of  $\pm 4.5$  meV around the Fermi energy, which is determined by the position of the bulk Weyl nodes. Six Fermi arcs connecting the projected Weyl nodes of opposite chirality are visible, confirming the existence of the WSM phase in these two solid-solution systems. Note that because of the small projected bulk gap on the loops where the Fermi arcs reside, some non-negligible spectral weight is visible even outside the Fermi arcs in Fig. 6, coming from the artificial smearing of the Green's functions.

#### 5. Simplified six-band model

In order to capture the essential physics in these materials, we construct a six-band TB model to describe the interesting critical behavior. From the band-structure plots presented in Fig. 7, it is clear that the band inversion occurs around the  $Z$  point of  $\text{LaBiTe}_3$  and  $\text{LuBiTe}_3$ , so we focus our attention on the six states at  $Z$  closest to the Fermi level. A symmetry analysis shows that these six states belong to two copies of the two-dimensional  $Z_6$  irreducible representation (irrep) of the  $C_{3v}$  group at  $Z$ , plus a Kramers pair of one-dimensional complex-conjugate  $Z_4$  and  $Z_5$  irreps corresponding to linear combinations of  $j_z = \pm 3/2$  orbitals.

We thus build our six-band TB model out of basis states having the symmetry of  $|p_z, \uparrow\rangle$  and  $|p_z, \downarrow\rangle$  on the Te atoms at the top and bottom of the quintuple layer, and

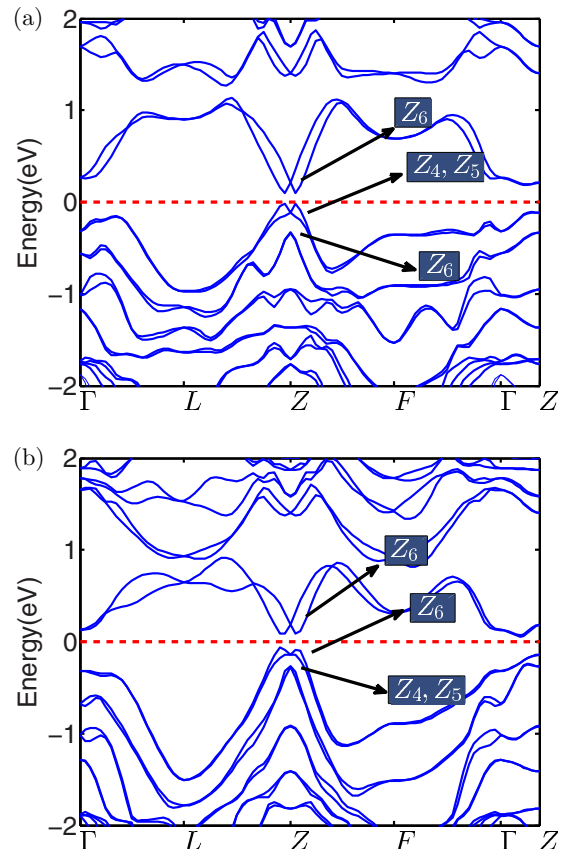


FIG. 7. (Color online) Bulk band structures of (a)  $\text{LaBiTe}_3$  and (b)  $\text{LuBiTe}_3$ .

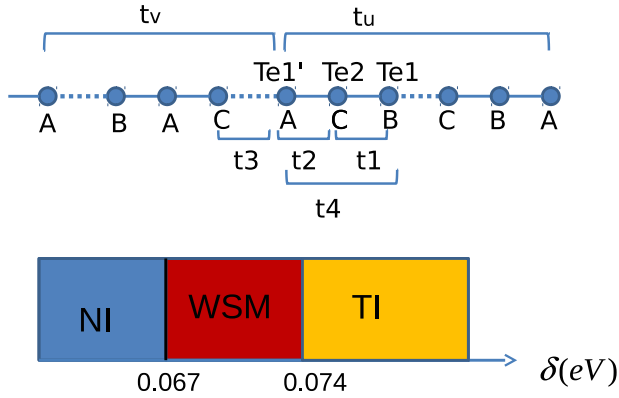


FIG. 8. (Color online) Top: Schematic diagram of the interlayer spin-independent hopping terms in the six-band model. Orbitals on sites Te1, Te2, and Te1' make up a quintuple layer; A, B, and C label in-plane hexagonal positions. Bottom: Phase diagram for the topological behavior of the six-band model.

$|p_x + ip_y, \uparrow\rangle$  and  $|p_x - ip_y, \downarrow\rangle$  combinations located on the central Te atoms. A schematic illustration of the six-band model is shown in Fig. 8, where the top, bottom, and central Te atoms are denoted by Te1, Te1', and Te2, respectively. First of all, six interlayer spin-independent hopping terms are included in the model. As shown in Fig. 8, we consider the first-neighbor hopping between the central and top (bottom) Te atoms  $t_1$  ( $t_2$ ), the inter-QL (intra-QL) hopping between the top and bottom Te atoms  $t_3$  ( $t_4$ ), and some further-neighbor hoppings  $t_u$  and  $t_v$  that are crucial in obtaining a nontrivial  $\mathbb{Z}_2$  index. Second, to capture the Rashba spin-splitting in the first-principles band structure, in-plane Rashba-like spin-dependent hoppings within the top and bottom Te monolayers are included and are denoted by  $\lambda_1$  and  $\lambda_2$ , respectively. For completeness, the interlayer first-neighbor Te1-Te2 ( $\lambda_3$ ) and Te1'-Te2 ( $\lambda_4$ ) Rashba-like hopping terms are also included. Lastly, to reproduce the first-principles band structure better, we also introduce first-neighbor spin-independent hopping terms within the Te1, Te2, and Te1' monolayers, denoted by  $v_1$ ,  $v_2$ , and  $v_3$ , respectively. The on-site energies are also different and are labeled by  $E_1$  for Te1,  $E_2$  for Te2, and  $E_3$  for Te1'. As our model is only intended to be semiquantitative, we use the same model parameters to describe both LaBiTe<sub>3</sub> and LuBiTe<sub>3</sub>.

We take all of the parameters in the model to depend on a scaling parameter  $\delta$  that drives the TPT. When  $\delta$  is zero, the system is a trivial insulator; as  $\delta$  increases, the system becomes a topological insulator by going through a critical WSM. The dependence of the parameters on  $\delta$  defines a path in parameter space. It is important to note that the width of the critical WSM region can be highly sensitive to this path, with an improper choice sometimes leading to an extremely narrow WSM phase. Our choice is specified in Table I.

Following the path we have chosen, a WSM phase is obtained for  $0.067 \text{ eV} < \delta < 0.074 \text{ eV}$ . As shown in Fig. 9(b), the smallest direct band gap in the BZ vanishes when  $0.067 \text{ eV} < \delta < 0.074 \text{ eV}$ , indicating the existence of BTPs in BZ. If one further checks the position of the BTPs, one finds that when  $\delta \approx 0.067 \text{ eV}$ , six quadratic BTPs are created in the mirror planes, which then split into 12 Weyl nodes and propagate in the BZ following the solid black and dashed red lines in

TABLE I. Parameters of the six-band model (in eV).

$t_1$	$0.2 - \delta/4$	$\lambda_3$	$0.15 - \delta/2$	$v_3$	0
$t_2$	$0.15 - \delta/4$	$\lambda_4$	$0.12 - \delta/2$	$E_1$	$0.1 + \delta - 6v_1$
$t_3$	$\delta$	$t_u$	$0.12 + \delta/2$	$E_2$	$-6v_2$
$t_4$	$0.1 - \delta/4$	$t_v$	$0.06 - \delta/2$	$E_3$	$-0.1 - \delta$
$\lambda_1$	$0.24 - \delta/2$	$v_1$	0.05		
$\lambda_2$	$0.2 - \delta/2$	$v_2$	0.1		

Figs. 9(c) and 9(d). These Weyl nodes eventually annihilate with each other at  $\delta \approx 0.074 \text{ eV}$  after exchanging partners, which qualitatively reproduces the phase-transition behavior of the VCA effective Hamiltonians very well. When  $\delta > 0.074 \text{ eV}$ , the system becomes a strong TI. The bulk band structure at  $\delta = 0.09 \text{ eV}$  in the TI phase is shown in Fig. 9(a), which very well captures the low-energy dispersions around Z that were found in the first-principles calculations.

## 6. Discussion

To conclude this section, we would like to comment that the width of the WSM phase depends on two ingredients. On one hand, as discussed above, it depends on the symmetry of the system; other things being equal, the WSM interval tends to be wider in systems with lower symmetry. On the other hand, even for fixed symmetry, it also depends on the detailed choice of path connecting the topological and trivial phases. Choosing a different path may broaden or reduce the WSM region. For example, if one artificially changes the strength of the atomic SOC strength in LaBiTe<sub>3</sub> and LuBiTe<sub>3</sub> in the Wannierized TB models, and scales the variation of the actual atomic SOC by a single scaling parameter  $\lambda$ , then we find

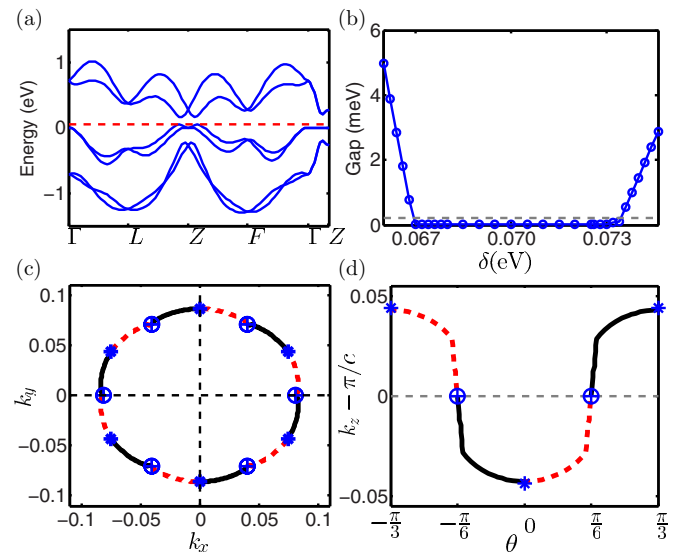


FIG. 9. (Color online) (a) Bulk bandstructure of the six-band model at  $\delta = 0.09 \text{ eV}$ . (b) Smallest direct band gap in the BZ vs.  $\delta$ . (c) Trajectory of Weyl nodes projected onto the  $(k_x, k_y)$  plane. Dashed red (solid black) line refers to the Weyl node with positive (negative) chirality. The “\*” and “⊕” denote the creation and annihilation point of the Weyl nodes respectively.  $\theta$  is the azimuthal angle in the  $(k_x, k_y)$  plane. (d) Trajectory of Weyl nodes along  $k_z$ . Units of  $k_x$ ,  $k_y$  and  $k_z$  are  $\text{\AA}^{-1}$ .

that the WSM region only shows up for  $\lambda$  in the range of 76.8%–77.3%, which is significantly narrower than for the VCA case. However, if an average SOC is applied to the entire system, such that the SOC strength on Te is artificially high and that on Bi is artificially low, we find that a much wider WSM region results. Thus, it may potentially be possible to engineer the width of a critical WSM phase if one can modify the transformation path, as by epitaxial strain, pressure, or additional chemical substitution.

### B. BiTeI: Revisited

In order to justify the discussion in Sec. II B, we revisit the TPT in BiTeI driven by pressure. In our calculations, the pressure is applied by compressing the volume of the primitive cell. The fully compressed volume  $V$  is taken to be 85.4% of the original volume  $V_0$ , such that the former is well inside the topological region [20], and both the lattice vectors and atomic positions are relaxed at the compressed volume. As discussed in Sec. III B, we searched for BTPs over the entire irreducible BZ for a transitional Hamiltonian scaled as  $H(\eta) = (1 - \eta)H_0 + \eta H_1$  for  $0 \leq \eta \leq 1$ , where  $H_0$  and  $H_1$  represent the Hamiltonians of the uncompressed and fully compressed BiTeI, with even and odd  $\mathbb{Z}_2$  indices, respectively. As shown in Fig. 10(a), as the pressure is increased from 0% to 100% (alternatively, as  $V$  is decreased from 100% to 85.4% of  $V_0$ ), a semimetallic phase emerges for  $\eta$  in the range of about 54%–56%.

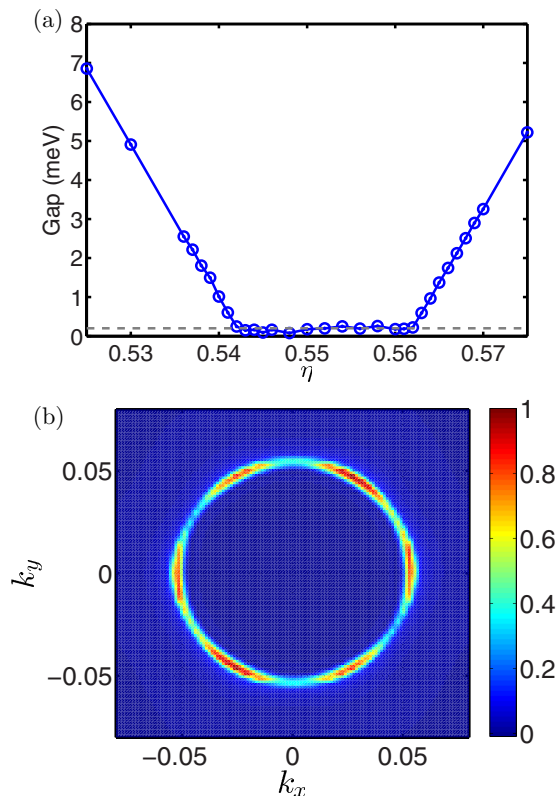


FIG. 10. (Color online) (a) Smallest direct band gap in the BZ of BiTeI vs the pressure-scaling variable  $\eta$ . (b) Surface spectral function of BiTeI in the WSM phase (at 55% of the full pressure).

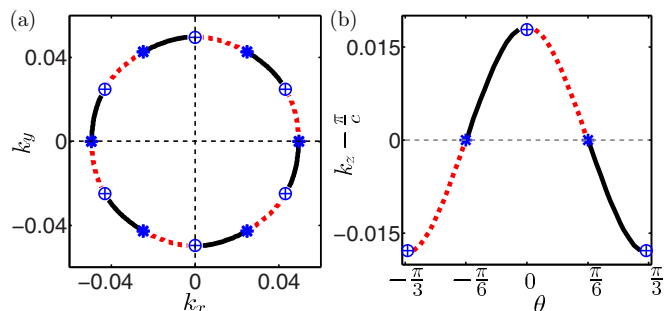


FIG. 11. (Color online) (a) Trajectories of Weyl nodes in the  $(k_x, k_y)$  plane (in units of  $\text{\AA}^{-1}$ ). Dashed red (solid black) lines indicate the trajectories of Weyl nodes with positive (negative) chirality. The “\*” and “⊕” denote the creation and annihilation point of the Weyl nodes, respectively. (b) Trajectory of Weyl nodes in the  $k_z$  direction (units of  $\text{\AA}^{-1}$ ).

The point group of BiTeI is the same as for LaBiTe<sub>3</sub> and LuBiTe<sub>3</sub>, namely,  $C_{3v}$ . Therefore, as explained in Sec. IV A, one would expect the emergence of 12 Weyl nodes in the entire BZ during the phase-transition process. The trajectories of the Weyl nodes are plotted in Figs. 11(a) and 11(b). When  $\eta \approx 54\%$ , six quadratic BTPs are first created at the BZ boundary  $k_z = \pi/c$  in the  $k_y = 0$  and other equivalent high-symmetry planes. These BTPs then split into 12 Weyl nodes which propagate along the directions indicated by solid black (antimonopoles) and dashed red (monopoles) lines. They annihilate each other in the three mirror planes after exchanging partners. Note that in this case the system goes from a normal to topological insulator as  $\eta$  increases, which is the reverse of the LaBi<sub>1-x</sub>Sb<sub>x</sub>Te<sub>3</sub> and LuBi<sub>1-x</sub>Sb<sub>x</sub>Te<sub>3</sub> cases.

The results shown in Fig. 11 support our conclusions in Sec. II B. In particular, even though the torsion argument implies that the trajectories of the two Weyl nodes which split off from a given quadratic BTP would never meet each other, a closed curve is still formed in the 3D BZ of BiTeI through the interchange of partners among the Weyl nodes.

Figure 10(b) shows the surface spectral function of BiTeI averaged around the Fermi level for  $\eta = 0.55$ , in the WSM phase. It is clear that there are six Fermi arcs extending between the six pairs of projected Weyl nodes, which is again the hallmark of a WSM phase.

We therefore conclude that a WSM phase does exist in the TPT of BiTeI, but it occurs only within a narrow pressure range. If  $\eta$  is changed by 2.5%, the volume is only changed by 0.39%, which might be difficult to measure experimentally. Again, the narrowness of the WSM interval can be attributed in part to the high symmetry of the system. However, as emphasized in the previous section, the width of the critical WSM is also sensitive to the choice of path in parameter space. The critical WSM could get broadened by choosing a different path, as for example by applying uniaxial pressure. We leave this for a future study.

### V. SUMMARY

In this paper, we have investigated the nature of the TPT in a noncentrosymmetric TI in the most general case. We find

that an intermediate WSM phase is always present, regardless of other lattice symmetries, as long as inversion symmetry is absent. We discussed separately the cases in which the Jacobian matrix is rank one or rank two when the gap first closes. In the rank-two case, each quadratic BTP would always split into a pair of Weyl nodes, which annihilate each other after exchanging partners. If the rank of the Jacobian is one, then the doubly quadratic BTP in this case would either split into four Weyl nodes, or else immediately be gapped out again, corresponding to an “insulator-insulator transition.” However, in the latter case, the bulk  $\mathbb{Z}_2$  indices are not expected to change. Therefore, we conclude that  $\mathbb{Z}_2$ -even and  $\mathbb{Z}_2$ -odd phases of a noncentrosymmetric insulator must always be separated by a region of WSM phase, even if other symmetries are present.

To illustrate our conclusions, we have carried out calculations on specific noncentrosymmetric insulators. For  $\text{LaBi}_{1-x}\text{Sb}_x\text{Te}_3$  and  $\text{LuBi}_{1-x}\text{Sb}_x\text{Te}_3$  we have used Wannierized VCA Hamiltonians to find a WSM phase in the region  $x \approx 38.5\%–41.9\%$  and  $x \approx 40.5\%–45.1\%$ , respectively. A six-band TB model was also constructed to describe the topological and critical behavior in these materials. We found that the width of the critical WSM phase can be highly sensitive to the choice of path in the parameter space, suggesting that there is flexibility to engineer the WSM phase.

We have also revisited the TPT of  $\text{BiTeI}$  as a function of pressure, where previous work suggested the absence of a WSM phase [19]. Using a carefully constructed algorithm to search for the minimum gap in the full three-dimensional BZ, we found that a WSM phase is indeed present over a narrow interval of pressure, although this range may be so narrow as to make its experimental observation difficult.

In summary, we have clarified the theory of a general  $\mathbb{Z}_2$ -even to  $\mathbb{Z}_2$ -odd topological phase transition in a three-dimensional time-reversal-invariant insulator with broken inversion symmetry, and demonstrated that an intermediate WSM phase must always be present. We have also detailed the behavior of  $\text{LaBi}_{1-x}\text{Sb}_x\text{Te}_3$  and  $\text{LuBi}_{1-x}\text{Sb}_x\text{Te}_3$  as promising candidates for WSMs of this kind. While we have not considered disorder or interactions explicitly, we expect our conclusions to survive at least for weak disorder or interactions. Our work is a step forward in the general understanding of topological phase transitions, and may provide useful guidelines for the experimental realization of new classes of Weyl semimetals.

#### ACKNOWLEDGMENT

This work is supported by NSF Grants No. DMR-10-05838 and No. 14-08838.

- 
- [1] K. v. Klitzing, G. Dorda, and M. Pepper, *Phys. Rev. Lett.* **45**, 494 (1980).
- [2] D. J. Thouless, M. Kohmoto, M. P. Nightingale, and M. den Nijs, *Phys. Rev. Lett.* **49**, 405 (1982).
- [3] M. Z. Hasan and C. L. Kane, *Rev. Mod. Phys.* **82**, 3045 (2010).
- [4] X.-L. Qi and S.-C. Zhang, *Rev. Mod. Phys.* **83**, 1057 (2011).
- [5] H. B. Nielsen and M. Ninomiya, *Phys. Lett. B* **130**, 389 (1983).
- [6] A. A. Burkov, M. D. Hook, and L. Balents, *Phys. Rev. B* **84**, 235126 (2011).
- [7] X. Wan, A. M. Turner, A. Vishwanath, and S. Y. Savrasov, *Phys. Rev. B* **83**, 205101 (2011).
- [8] A. M. Turner and A. Vishwanath, in *Topological Insulators*, edited by M. Franz and L. Molenkamp (Elsevier, Amsterdam, 2013), Chap. 11, pp. 293–322.
- [9] P. Hosur and X. Qi, *C. R. Phys.* **14**, 857 (2013).
- [10] R. Okugawa and S. Murakami, *Phys. Rev. B* **89**, 235315 (2014).
- [11] K.-Y. Yang, Y.-M. Lu, and Y. Ran, *Phys. Rev. B* **84**, 075129 (2011).
- [12] A. A. Burkov and L. Balents, *Phys. Rev. Lett.* **107**, 127205 (2011).
- [13] F. D. M. Haldane, [arXiv:1401.0529](https://arxiv.org/abs/1401.0529).
- [14] A. A. Zyuzin and A. A. Burkov, *Phys. Rev. B* **86**, 115133 (2012).
- [15] V. Aji, *Phys. Rev. B* **85**, 241101 (2012).
- [16] D. Bulmash, C.-X. Liu, and X.-L. Qi, *Phys. Rev. B* **89**, 081106 (2014).
- [17] S. Murakami and S.-i. Kuga, *Phys. Rev. B* **78**, 165313 (2008).
- [18] S. Murakami, *New J. Phys.* **9**, 356 (2007).
- [19] B.-J. Yang, M. S. Bahramy, R. Arita, H. Isobe, E.-G. Moon, and N. Nagaosa, *Phys. Rev. Lett.* **110**, 086402 (2013).
- [20] M. Bahramy, B.-J. Yang, R. Arita, and N. Nagaosa, *Nat. Commun.* **3**, 679 (2012).
- [21] B. Yan, H.-J. Zhang, C.-X. Liu, X.-L. Qi, T. Frauenheim, and S.-C. Zhang, *Phys. Rev. B* **82**, 161108 (2010).
- [22] X. Xi, C. Ma, Z. Liu, Z. Chen, W. Ku, H. Berger, C. Martin, D. B. Tanner, and G. L. Carr, *Phys. Rev. Lett.* **111**, 155701 (2013).
- [23] A. A. Soluyanov and D. Vanderbilt, *Phys. Rev. B* **83**, 235401 (2011).
- [24] K. Ishizaka, M. Bahramy, H. Murakawa, M. Sakano, T. Shimojima, T. Sonobe, K. Koizumi, S. Shin, H. Miyahara, A. Kimura, K. Miyamoto, T. Okuda, H. Namatame, M. Taniguchi, R. Arita, N. Nagaosa, Y. Kobayashi, K. Murakami, R. Kumai, Y. Kaneko, Y. Onose, and Y. Tokura, *Nat. Mater.* **10**, 521 (2011).
- [25] G. Kresse and J. Furthmüller, *Phys. Rev. B* **54**, 11169 (1996).
- [26] G. Kresse and J. Furthmüller, *Comput. Mater. Sci.* **6**, 15 (1996).
- [27] J. P. Perdew, K. Burke, and M. Ernzerhof, *Phys. Rev. Lett.* **77**, 3865 (1996).
- [28] J. P. Perdew, K. Burke, and M. Ernzerhof, *Phys. Rev. Lett.* **78**, 1396 (1997).
- [29] H. J. Monkhorst and J. D. Pack, *Phys. Rev. B* **13**, 5188 (1976).
- [30] A. A. Mostofi, J. R. Yates, Y. S. Lee, I. Souza, D. Vanderbilt, and N. Marzari, *Comput. Phys. Commun.* **178**, 685 (2008).
- [31] The TB models from WANNIER90 are realistic in the sense that the Wannier-interpolated band structure can reproduce the first-principles band energies exactly in a specified energy window which is chosen here to be centered around the Fermi level.
- [32] J. Liu and D. Vanderbilt, *Phys. Rev. B* **88**, 224202 (2013).
- [33] The fully occupied  $f$  shell of Lu has very little influence on the electronic structure around the Fermi level.
- [34] N. Marzari and D. Vanderbilt, *Phys. Rev. B* **56**, 12847 (1997).
- [35] I. Souza, N. Marzari, and D. Vanderbilt, *Phys. Rev. B* **65**, 035109 (2001).
- [36] M. L. Sancho, J. L. Sancho, J. L. Sancho, and J. Rubio, *J. Phys. F* **15**, 851 (1985).